



HAL
open science

Variational entropy generation minimization of a channel flow: Convective heat transfer in a gas flow

J.M. Avellaneda, F. Bataille, A. Toutant, G. Flamant

► To cite this version:

J.M. Avellaneda, F. Bataille, A. Toutant, G. Flamant. Variational entropy generation minimization of a channel flow: Convective heat transfer in a gas flow. *International Journal of Heat and Mass Transfer*, 2020, 160, pp.120168. 10.1016/j.ijheatmasstransfer.2020.120168 . hal-03523234

HAL Id: hal-03523234

<https://univ-perp.hal.science/hal-03523234>

Submitted on 22 Aug 2022

HAL is a multi-disciplinary open access archive for the deposit and dissemination of scientific research documents, whether they are published or not. The documents may come from teaching and research institutions in France or abroad, or from public or private research centers.

L'archive ouverte pluridisciplinaire **HAL**, est destinée au dépôt et à la diffusion de documents scientifiques de niveau recherche, publiés ou non, émanant des établissements d'enseignement et de recherche français ou étrangers, des laboratoires publics ou privés.



Distributed under a Creative Commons Attribution - NonCommercial 4.0 International License

Variational entropy generation minimization of a channel flow: convective heat transfer in a gas flow

J.M. Avellaneda^{a,*}, F. Bataille^a, A. Toutant^a, G. Flamant^b

^aPROMES-CNRS, UPR 8521, University of Perpignan Via Domitia, Perpignan, France

^bPROMES-CNRS, UPR 8521, 7 rue du Four solaire, 66120 Font Romeu, France

Abstract

Variational methods are used to optimize convective heat transfer in a channel gas flow. The minimization of a functional objective combining the rate of total entropy generation in the channel on the one hand and the total viscous dissipation on the other hand results in velocity and temperature fields. A weighting factor allows varying the relative importance of these two terms and a virtual body force field is applied to vary the velocity field pattern via the momentum equation source term. The result is velocity configurations that minimize the objective functional. This study shows that the velocity fields determined by the optimization process effectively lead to a reduction in the entropy generation rate in the flow as well as a reduction in the temperatures of the heated plate. In addition, the value of the weighting factor triggers the transition from slightly to highly perturbed velocity and temperature fields when compared to a non-optimized flow. The heat transfer enhancement is assessed and the increase of the Nusselt number is put in perspective with the reduction of the entropy generation rate and the increase of viscous friction. The results could be used to design passive technologies for enhancing wall-to-fluid heat transfer.

Keywords: Second law, Optimization, Variational analysis, Entropy minimization

1. Introduction

Improving heat transfer in convective flows is a vast and active area of research that has applications in many industrial fields like nuclear [1] or solar [2] [3] [4] [5] [6] [7] power plants, process industry [8], chemical engineering [9], air-conditioning or cooling of electronic systems [10] and automotive [11] or aerospace [12] industries to name but a few. To enhance heat transfer many methods have been studied, generally classified according to whether they are active, passive or using a combination of the latter. Active methods require external energy supply to maintain the enhancement mechanism [13]: they can be based upon ultrasound [14], wall morphing [15] [16] and vibrating walls [17] including piezoelectric fans, impingement jets [18] [19] or sprays [20] [21], and electric field force on a dielectric fluid [22]. Heat transfer improvement passive methods are based upon three main techniques. Inserts can be placed in the fluid path to extend the exchange surface, redirect

the flow, break boundary layers and promote mixing, swirl, vortexes and turbulence. There is a wide variety of inserts [23] [24]: twisted tapes, coiled wires, conical rings, helical screws and also fins, baffles or ribs. Combinations of techniques such as perforated twisted tapes or those with cut or corrugated edges have also been studied. Another passive method consists in using coatings or surface roughening [25] [26]. Finally, improving heat transfer can also be performed by changing the characteristics of the fluid (its heat capacity, viscosity and thermal conductivity), one active area of research being the use of nanofluids [27, 28, 29] (i.e. a fluid containing nanoparticles, whose sizes are < 100 nm). Nanoparticles can be made of a metal (e.g. Au or Cu), a metal oxide (e.g. TiO_2 , Fe_3O_4 , CuO, Al_2O_3) or other chemical substances (e.g. SiC, Carbon nanotubes) dispersed in a fluid, in particular: water, oil, molten salts or ethylene-glycol. The use of nanoparticles can be combined with passive [30] methods and applied for example in the nuclear [31] or solar industry [32]. Higher size (micro-metric) particle suspensions are also promising to improve the performance of concentrated solar power plants [33] [34] [35].

Whatever the method used to increase heat exchange,

*Corresponding author

Email address: jean-marc.avellaneda@promes.cnrs.fr
(J.M. Avellaneda)

it is necessary to ensure that this improvement is not accompanied by the harmful degradation of another performance criterion. In particular, one of the challenges in optimizing forced convective heat transfers is the balance between intensifying thermal exchange while minimizing or controlling pressure drop increase, both having to be taken into account [36] [37]. One way to address this trade-off consists in minimizing the entropy generation rate, which includes all the available power lost due to irreversibility in the flow whether it comes from the viscous friction responsible for the pressure drop or from the conduction phenomena through finite temperature differences [38] [39] [40]. As total viscous dissipation is related to the drop in pressure that can be a constrained element in industrial applications, it is also interesting to seek a minimization of the entropic power generated while maintaining control of total viscous dissipation [41] [42], which can be done by using a weighted objective functional.

In this study, we consider situations where the entropy generation rate by heat transfer is largely dominant when related to the viscous friction entropy generation rate (which corresponds to $Be \approx 1$, where Be is the thermodynamic Bejan number [43]). We look for velocity and temperature fields that minimize a functional objective combining the entropy generation rate by the overwhelmingly dominant factor (i. e. heat conduction) on the one hand and the total viscous dissipation on the other hand, the latter being weighted by a factor that can be freely fixed in order to give more or less weight to the pressure drop in the optimization process. Several simulations were carried out for three Reynolds number values, by varying this total viscous dissipation weighting factor, in order to observe its influence on the entropy generation rates as well as on key physical variables such as the temperature of the heated wall, the total viscous dissipation, the maximum temperature and velocity in the channel and the outlet mean temperature.

2. Numerical method

2.1. Governing equations

We consider the two-dimensional steady-state incompressible flow of a Newtonian fluid with constant properties. Viscous heating and gravity are neglected and there is no source term in the energy equation nor any radiative exchange. Taking into account these assumptions, the conservation of mass, momentum and energy lead respectively to the following equations [44]:

$$\nabla \cdot \mathbf{V} = 0 \quad (1)$$

$$\rho \mathbf{V} \cdot \nabla \mathbf{V} = -\nabla P + \mu \nabla^2 \mathbf{V} + \mathbf{F} \quad (2)$$

$$\mathbf{V} \cdot \nabla T = \frac{k}{\rho C_p} \nabla^2 T \quad (3)$$

In this set of equations, \mathbf{V} is the velocity vector of the fluid, $\rho = 1.177 \text{ kg.m}^{-3}$ its density, P its pressure, $\mu = 1.846 \times 10^{-5} \text{ Pa.s}$ its dynamic viscosity, T its temperature, $k = 0.02624 \text{ W.m}^{-1} \cdot \text{K}^{-1}$ its thermal conductivity, $C_p = 1004.9 \text{ J.kg}^{-1} \cdot \text{K}^{-1}$ its thermal capacity at constant pressure and \mathbf{F} is a volume force field that will be used in the optimization process described below. The body force \mathbf{F} can be considered as a virtual force field allowing to vary the velocity field pattern via the momentum equation source term to find the velocity configuration that minimizes the objective functional. The practical implementation of the resulting optimal velocity field can be approached by passive means, such as baffles positioned in the fluid path, or by the use of porous material structures as described in [41] and [45].

Viscous heating is neglected in the heat equation (Eq. 3) as the simulations are done for very low values of the Brinkman number ($Br \approx 10^{-5} \ll 1$) [46]. The Brinkman number $Br = PrEc$, where Ec is the Eckert number, appears explicitly when the heat equation is written in dimensionless form [47] and accounts for the relative importance of the viscous dissipation term when compared to the conductive heat term. Viscous heating would not be negligible for high Mach number flows [48], very narrow channels [49] in particular for liquid flows [50] or very viscous fluids like oils [51] or polymers.

The local entropy generation rate (by unit of volume, which is symbolized by a three-prime superscript) in the case of a homogeneous, non-reactive and electrically non-conductive fluid can be calculated using the following expression, where Φ is the viscous dissipation function [38]:

$$\dot{S}_{gen}''' = \frac{k}{T^2} (\nabla T)^2 + \frac{\Phi}{T} \quad (4)$$

$$\Phi = \mu \left\{ 2 \left[\left(\frac{\partial u}{\partial x} \right)^2 + \left(\frac{\partial v}{\partial y} \right)^2 \right] + \left(\frac{\partial u}{\partial y} + \frac{\partial v}{\partial x} \right)^2 \right\} \quad (5)$$

This general expression consists in two terms. As stated before, in the present study the viscous dissipation term Φ is negligible in the energy equation. Moreover, the integral of Φ/T over the fluid domain is also negligible in the entropy generation rate when compared to the integral of the entropy generation rate by heat transfer $\frac{k}{T^2} (\nabla T)^2$.

2.2. Variational problem

Finding a minimum of a linear combination of the following two terms (Ω being the control volume) results in minimizing the generation of entropy by heat conduction while taking into account the total viscous dissipation:

$$J = \iiint_{\Omega} \left(\frac{k}{T^2} (\nabla T)^2 + W_{\Phi} \Phi \right) d\Omega \quad (6)$$

In Eq. 6, W_{Φ} is a weighting factor allowing to control the relative importance given to the viscous dissipation. Using two positive weighting factors in the objective functional, one for the thermal term (W_{th}) and the other one for the viscous dissipation term (W_{visc}) would result in the same optimized velocity and temperature fields than using Eq. 6 with $W_{\Phi} = W_{visc}/W_{th}$ because W_{Φ} represents the relative weight given to the viscous dissipation vs. the entropy generation rate in the optimization. As already stated, the viscous dissipation term is negligible in the entropy generation rate when compared to the entropy generation rate by heat transfer. Consistently, the objective functional (Eq. 6) takes into account the entropy generation by integrating only the heat transfer term $\frac{k}{T^2} (\nabla T)^2$, the term Φ/T in Eq. 4 being dropped. The second term of the objective functional is $W_{\Phi} \Phi$, i.e., the product of the weighting factor W_{Φ} by the viscous dissipation (which integral corresponds to the total mechanical power to supply in order to maintain the flow).

The constraints expressed by the mass and energy conservation equations (Eqs. 1 and 3) are taken into account through two Lagrange multipliers (respectively λ_1 and λ_2 that are functions of the x and y coordinates). This leads to the following Lagrangian criterion to minimize:

$$J^* = \iiint_{\Omega} \left\{ \frac{k}{T^2} (\nabla T)^2 + W_{\Phi} \Phi + \lambda_2 \left[\frac{k}{\rho C_p} \nabla^2 T - \mathbf{V} \cdot \nabla T \right] + \lambda_1 \nabla \cdot \mathbf{V} \right\} d\Omega \quad (7)$$

The expression of the volume force field is obtained by equaling to zero the first variation of J^* with respect to the components u and v of the velocity in order to deduce the corresponding Euler-Lagrange equations and taking into account the equation of the conservation of momentum (Eq. 2):

$$\mathbf{F} = \frac{\lambda_2}{2W_{\Phi}} \nabla T + \rho \mathbf{V} \cdot \nabla \mathbf{V} \quad (8)$$

Making the first variation of J^* with respect to T vanish leads to a transport-like equation for the λ_2 Lagrange multiplier:

$$\nabla \cdot \left(\rho \mathbf{V} \lambda_2 - \frac{-k}{C_p} \nabla \lambda_2 \right) = \frac{2k\rho}{T} \nabla \cdot \left(\frac{\nabla T}{T} \right) \quad (9)$$

The boundary conditions applicable to equation Eq. 9 depend on those concerning the temperature: if the temperature is imposed on a boundary of the domain, Eq. 10 applies and if the heat flux density is imposed, Eq. 11 must be taken into account (where $\partial/\partial n$ is the normal derivative to the boundary):

$$\lambda_2 = 0 \quad (10)$$

$$\frac{\partial \lambda_2}{\partial n} = \frac{2\rho C_p}{T^2} \frac{\partial T}{\partial n} \quad (11)$$

Finally, the differential equation system to be solved consists in Eqs. 1 to 3 (supplemented by boundary conditions for temperature, velocity and/or pressure) and Eqs. 8 and 9 (supplemented by the boundary conditions in Eqs. 10 or 11). The λ_1 Lagrange multiplier is not necessary but can be computed by:

$$\nabla \lambda_1 = -2W_{\Phi} \nabla P \quad (12)$$

In the present study, \mathbf{F} is an unknown of the optimization problem to be determined in order to minimize the objective functional. To find \mathbf{F} , an approach could have consisted in starting from an initial body force field and to apply an iterative optimization technique to get close to the optimum force field [52]. This would have required a large number of resolutions of the governing equations and computations of the objective functional, especially since the unknown \mathbf{F} is here a vector field to be set for a large number of cells in the domain and not a simple real parameter. Moreover, the function J to be minimized is a functional (a function of functions) depending on fields (the velocity, the temperature and their derivatives) and not on mere real variables. Finally, the governing equations and the functional are non-linear. The calculus of variations allows to find directly the expression of the body force field that minimizes the objective functional (Eq. 8) by transforming the optimization problem into a set of Euler-Lagrange equations [53] [54]. The optimization is thus carried-out mathematically and not numerically. For each value of W_{Φ} in the objective functional a particular body force field is applied in the channel (Eq. 8) via the momentum equation (Eq. 2). The numerical resolution of the usual flow governing equations (Eqs. 1 to 3) combined with the expression of the body-force (Eqs. 8 and 9) and the

210 boundary conditions results in a unique velocity field
 and a unique temperature field. This set of equations is
 highly coupled as the body force field itself depends on
 the temperature and the velocity fields.

215 W_{Φ} can be considered as a weighting factor in a
 multi-objective optimization problem: minimizing the
 entropy generation rate and the pressure drop while
 these two objectives are often contradictory does not
 result in a single optimum. Using a weighting factor
 allows to find a wide range of trade-offs depending on
 220 the relative focus put on reducing the entropy genera-
 tion rate or the viscous dissipation. For high values of
 W_{Φ} , the emphasis is put on the reduction of pressure
 drop (and more precisely of the total viscous dissipa-
 tion, which corresponds to the mechanical power re-
 225 quired to maintain the flow). Conversely, small values
 of W_{Φ} correspond to a focus on minimizing the entropy
 generation rate in the channel. Each value of W_{Φ} leads
 to an optimal velocity field that minimizes differently
 the two contradictory objectives pursued since they are
 230 assigned different weighting factors. W_{Φ} is the key pa-
 rameter in the multi-objective optimization allowing to
 browse the spectrum of trade-offs between the solutions
 focused on the entropy generation and those where vis-
 cous dissipation has to be reduced or at least limited in
 235 its increase: this is why a large part of the results are
 presented as functions W_{Φ} in section 3.

2.3. Numerical model

240 The fluid is dry air, flowing between two transversely
 infinite flat plates (Fig. 1) that are impermeable and
 comply with the no-slip boundary condition. The walls
 are adiabatic except for the middle third of the lower
 245 wall that is subjected to a uniform and constant heat
 flux density (1000 W.m^{-2} for all simulations) over 1 cm
 length, which results in a 10 W heat flux added in the
 headed area. The domain dimensions are $30 \text{ mm} \times 5 \text{ mm}$
 and a uniform 1200×200 mesh is applied. At the inlet,
 250 the velocity and the temperature of the fluid are fixed
 and at the outlet, the gage pressure is set to zero. The
 atmospheric pressure is 101325 Pa . The average inlet
 gage pressure resulting from simulations varies from
 0.02 Pa to 1.76 Pa depending on the Reynolds number
 and the value of W_{Φ} .

255 The ANSYS Fluent 15.0 code is used to solve the
 flow equations with the SIMPLE velocity-pressure cou-
 pling algorithm. UDF scripts have been developed to
 solve the additional λ_2 equation (Eq. 9) and to define the
 \mathbf{F} volume force field that is applied in the central area of
 260 the domain (between $x = 10 \text{ mm}$ and $x = 20 \text{ mm}$) in or-
 der to avoid side effects and to keep simple inlet and out-
 let boundary conditions. For steady-state simulations,

the SIMPLE [55] or SIMPLEC pressure-velocity cou-
 pling methods are recommended [56]. PISO (Pressure-
 Implicit with Splitting of Operators algorithm) would
 be recommended for transient calculations or steady-
 state computations on highly skewed meshes, which is
 not the case in the present study. As the problem to
 be solved is complicated by the presence of a momen-
 tum source term (the body-force \mathbf{F} that furthermore de-
 pends on the solution of an additional partial differen-
 tial equation for the second Lagrange multiplier λ_2 in
 Eq. 9), the SIMPLEC algorithm, which could speed-
 up the calculations but may lead to more instability, has
 been discarded. ANSYS Fluent (14.5 or prior versions)
 and the SIMPLE pressure-velocity coupling algorithm
 have been used to solve fluid flow equations combined
 with additional scalar transport equations and with cus-
 tomized momentum and scalar source terms as reported
 in published studies dealing with mass transfer enhance-
 ment in laminar flow [45], chemical reaction optimiza-
 tion in reactive flow [57] [58] or convective heat trans-
 fer optimization in turbulent flow [41].

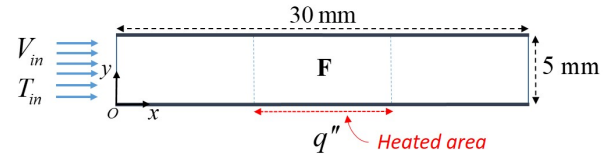


Figure 1: Domain characteristics.

For pressure and energy, second-order discretiza-
 tion schemes are applied. Momentum is solved with
 a QUICK scheme and λ_2 is solved with a first order
 scheme.

265 The dimensionless distance to the wall of the first re-
 solved point above the heated plate $y_1^+ = y_1 u_\tau / \nu$ (where
 u_τ is the friction velocity at the wall) increases with the
 Reynolds number and the weighting coefficient W_{Φ} and
 lies between $y_1^+ = 0.03$ and $y_1^+ = 0.26$. These posi-
 270 tions are all under $y_1^+ = 1$. Moreover $y_1 \sqrt{V_{in}/(\nu x_1)} < 1$
 (where x_1 is the abscissa of the first resolved point) even
 for the highest simulated Reynolds number, which al-
 lows to solve the boundary layer in the dynamically de-
 veloping entry length of the channel [59] [56]. Mesh
 independence has been checked with a two times finer
 mesh (2400×400) and is described hereunder.

275 About forty simulations were performed, divided into
 three groups corresponding to three Reynolds number
 (based upon the channel height): $Re = 20$, $Re = 30$
 and $Re = 320$, obtained by varying the inlet velocity
 V_{in} . In each group several values of the weighting factor
 W_{Φ} were tested, the global span of values ranging from

305 $W_{\Phi} \approx 0.5 K^{-1}$ to $W_{\Phi} \approx 1.2 \times 10^5 K^{-1}$ so as to provide a wide range of situations from cases where viscous dissipation is of significant importance in optimizing the objective functional to cases where its relative weight is a priori negligible. In all simulation the inlet temperature is set to $T_{in} = 300 K$: the optimization results in modified temperatures inside the channel and at the bottom plate in particular.

310 A mesh sensitivity analysis has been performed for $Re = 30$ with a 2400×400 mesh (twice as fine as the 1200×200 reference mesh). The entropy generation rates in the channel are changed by less than 1% and the variations of the entropy generation rate as a function of the weighting factor W_{Φ} are in good match for both mesh definitions (Fig. 2). Slightly and highly perturbed velocity and temperature fields (described in Section 3) are still observed with the same approximate critical value of $W_{\Phi, critical}$ triggering the transition between these two field patterns. As the results are practically mesh independent, using a finer mesh would lead to a marginal precision improvement with a significant increase in computer resource and time.

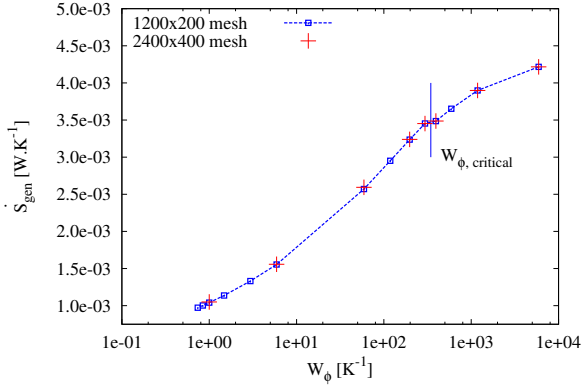


Figure 2: Total entropy generation rate for two mesh definitions. $Re = 30$

3. Results and discussion

330 In the following sections, the figures presenting the variation of various physical quantities as a function of W_{Φ} or $\Phi_{tot} = \int_{\Omega} \Phi . d\Omega$ combine points and dashed lines: each point correspond to the result of an effective simulation and dashed lines are used for readability and trend representation only.

3.1. Total entropy generation rates

335 As shown in Fig. 3, whatever the value of W_{Φ} , the optimized cases lead to a reduced total entropy genera-

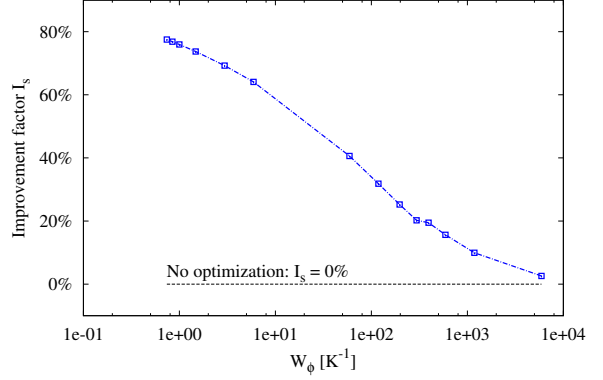


Figure 3: Improvement factor I_S (Eq. 13) as a function of W_{Φ} . $Re = 30$.

340 tion rate in the channel, when compared to the case with no optimization, the relative reduction being quantified by using an improvement factor I_S (Eq. 13) that is increasing when W_{Φ} decreases. For high values of W_{Φ} ($10^5 K^{-1}$ or more), the improvement factor is near zero. For $W_{\Phi} = 1 K^{-1}$, I_S is around 74% when $Re = 30$.

$$I_S = 1 - \frac{\dot{S}_{gen, optimized}}{\dot{S}_{gen, no optimization}} \quad (13)$$

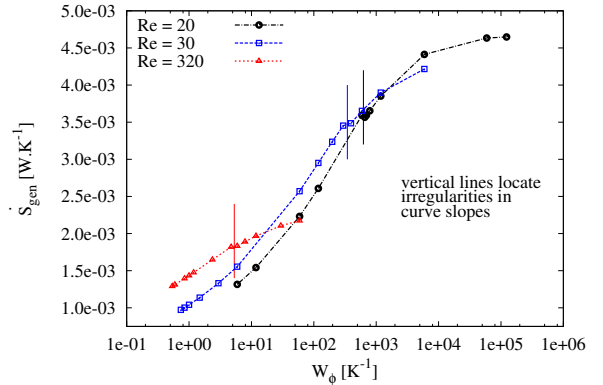


Figure 4: Total entropy generation rate \dot{S}_{gen} as a function of W_{Φ}

345 The total entropy generation rate increases with W_{Φ} (Fig. 4). For high values of W_{Φ} , the slope of the curve is small and approaches zero. The slope is higher for intermediate values of the weighting factor and it flattens when reaching small values of W_{Φ} . An unevenness of the slope also appears (it is embodied by vertical lines in Fig. 4), whose localization depends on the Reynolds number: the higher the Reynolds number, the lower the value of W_{Φ} for which this irregularity occurs (around

$W_{\Phi} = 325 K^{-1}$ if $Re = 30$ and around $W_{\Phi} = 5 K^{-1}$ when $Re = 320$).

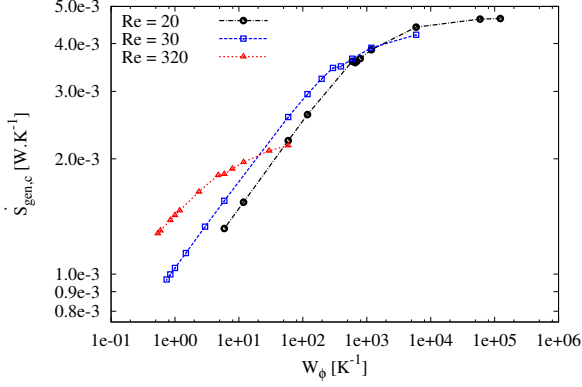


Figure 5: Entropy generation rate due to heat conduction $\dot{S}_{gen,c}$ as a function of W_{Φ}

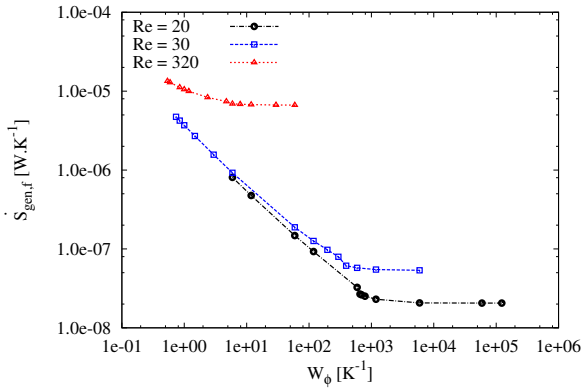


Figure 6: Entropy generation rate due to viscous friction $\dot{S}_{gen,f}$ as a function of W_{Φ}

The entropy generation rate in the channel is the sum of heat conduction ($\dot{S}_{gen,c}$, in Fig. 5) and viscous friction ($\dot{S}_{gen,f}$, in Fig. 6) contributions. The order of magnitude of the heat conduction part is the $mW.K^{-1}$ while the viscous part ranges between $\approx 10 nW.K^{-1}$ and $\approx 10 \mu W.K^{-1}$, depending on the Reynolds number. Because of the very small relative importance of the viscous part in comparison to the heat conduction part, the entropy generation rate by heat conduction is almost equal to the total entropy generation rate. The entropy generation rate by viscous friction (Fig. 6) is increasing when W_{Φ} decreases because the total viscous dissipation Φ_{tot} is increasing (Fig. 7), while the temperature remains in the order of 300 K. This means that the improvement observed on heat conduction entropy

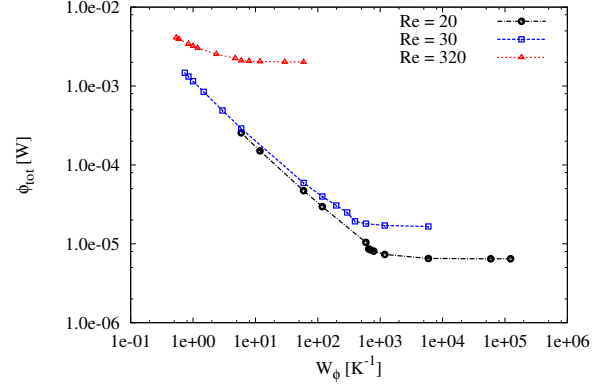


Figure 7: Total viscous dissipation $\Phi_{tot} = \int_{\Omega} \Phi . d\Omega$ as a function of W_{Φ}

generation (and on the total entropy generation rate) is gained at the expense of an increase of the total viscous dissipation and correlatively of the viscous entropy generation rate, which remains however relatively small.

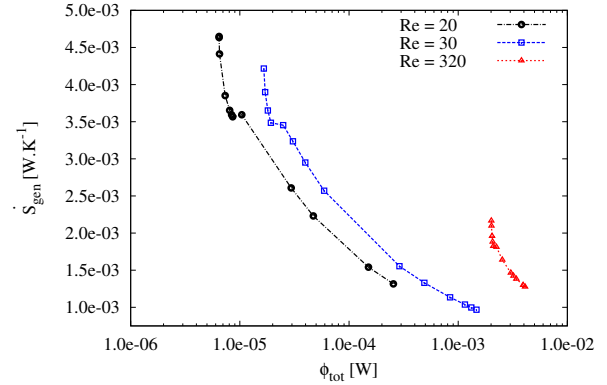


Figure 8: Total entropy generation rate \dot{S}_{gen} as a function of the total viscous dissipation Φ_{tot}

The decreasing behavior of the total entropy generation rate when the total viscous dissipation increases is even clearer when observing the direct relationship between these two physical integrals (Fig. 8). As $\dot{S}_{gen} \approx \iiint_{\Omega} \frac{k}{T^2} (\nabla T)^2 . d\Omega$, the entropy generation rate in the channel is essentially the consequence of the temperature distribution in the fluid domain, which comes from the velocity field that in turn depends on the body-force \mathbf{F} applied. The weighting factor plays a key role as it appears in the first term of the expression of the body-force in Eq. 8. Each chosen value of W_{Φ} leads to a different body-force \mathbf{F} and to a different velocity field (which determines the total viscous dissipation Φ_{tot}) and

385 a different temperature field (which determines the total entropy generation rate \dot{S}_{gen}). A decrease of W_{Φ} results in an increase of Φ_{tot} (because the velocities are higher) and a decrease of \dot{S}_{gen} (because the temperature is more homogeneous). As a result, the total entropy generation in the channel is decreasing function of the total viscous dissipation (Fig. 8). The pressure work is taken into account through the viscous dissipation Φ in the objective functional. From the steady-state balance of kinetic energy, one can deduce that $\Phi_{tot} = \int_{\Omega} \Phi \cdot d\Omega$ corresponds to the sum of the following terms: the pressure power, the body-force power, the viscous force power (acting at the inlet and the outlet of the channel, which is negligible) and the net increase of kinetic energy flux from the inlet to the outlet (that stays practically constant as the kinetic energy at the inlet is fixed and the velocity profile at the outlet is very close to the Poiseuille parabolic profile). While reducing the entropy generation rate through optimization, the total viscous dissipation increases (Fig. 8) by including the combination of pressure power and body-force power changes. For example, when $Re = 30$ and $W_{\Phi} = 200 K^{-1}$, the net increase in kinetic energy flux is $1.59 \times 10^{-6} W$ and is not significantly changed with respect to the case without optimization. On the other hand, Φ_{tot} is increased by $1.4 \times 10^{-5} W$, which corresponds to an increase of pressure power by $1.25 \times 10^{-5} W$ and an increase in body-force power by $0.15 \times 10^{-5} W$.

The viscous related quantities $\dot{S}_{gen,f}$ and Φ_{tot} in Figs. 6, 7 and 8 exhibit the irregularity already observed in Fig. 4, which is particularly visible when $Re = 20$ or $Re = 30$.

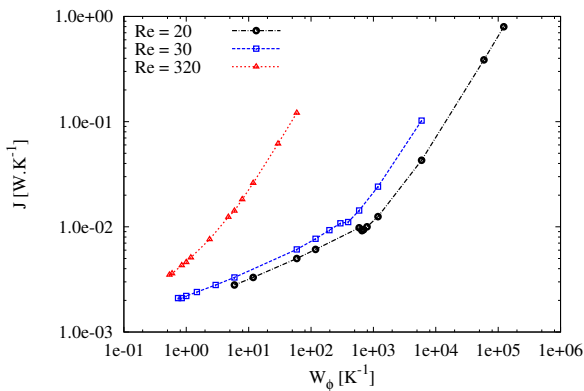


Figure 9: J objective functional as a function of W_{Φ}

The weighted objective functional J is an increasing function of W_{Φ} (see Fig. 9) even for high values of the weighting factor. Indeed, when W_{Φ} gets high in Eq. 6,

the entropy generation rate by heat conduction (Fig. 5) and the total viscous dissipation (Fig. 7) stabilize, while the weighting factor W_{Φ} increases.

3.2. Flow regimes

Depending on the value of W_{Φ} , the velocity and temperature fields exhibit different profiles [42], being more or less perturbed when compared to the case where no optimization is applied at all.

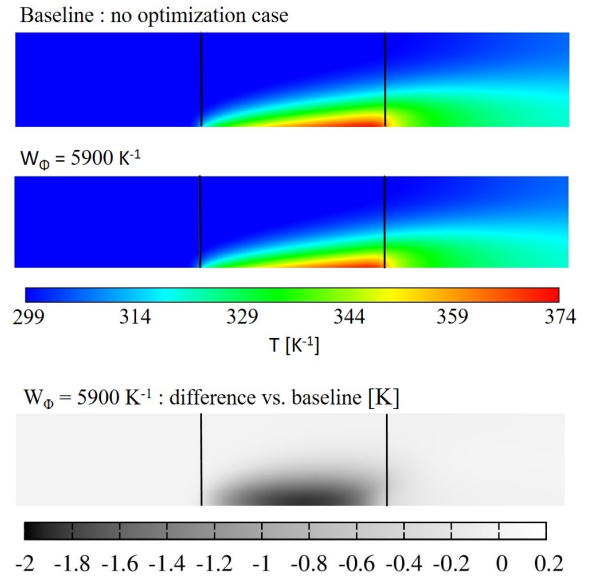


Figure 10: Temperature field with no optimization and when $W_{\Phi} = 5900 K^{-1}$. $Re = 30$. Differences with the baseline are in shades of gray.

For high values of W_{Φ} , for example $5900 K^{-1}$, the temperature and velocity fields are very similar to the case where no optimization is applied (see Figs. 10 and 11, where the abscissa at the beginning and end of the heated zone are materialized by two black vertical lines). Nevertheless, the optimization process has already an influence: when $Re = 30$, the maximum temperature in the channel without optimization is $373.5 K$ and $372.2 K$ when $W_{\Phi} = 5900 K^{-1}$.

For smaller values of W_{Φ} , the influence of the optimization process becomes more significant and the perturbation level (when compared to the case where no optimization is performed) increases as W_{Φ} decreases (see Figs. 12 and 13): if $W_{\Phi} = 400 K^{-1}$, the temperature profile exhibits a squeeze above the heated zone and this phenomenon becomes more pronounced as W_{Φ} decreases. At $W_{\Phi} = 300 K^{-1}$ and even more at $W_{\Phi} = 200 K^{-1}$, a protrusion (plume) appears above the beginning of the heated area.

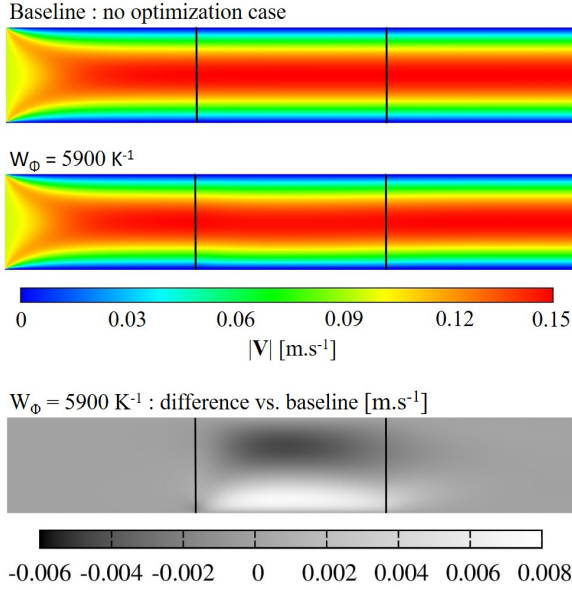


Figure 11: Velocity magnitude field with no optimization and when $W_{\phi} = 5900 K^{-1}$. $Re = 30$. Differences with the baseline are in shades of gray.

The velocity magnitude field at $W_{\phi} = 400 K^{-1}$ is also stuck towards the bottom plate and this observation is still valid when decreasing W_{ϕ} . Moreover, as W_{ϕ} gets smaller, areas of the channel exhibit higher velocities, in particular around the beginning of the heated zone (above a round structure circling an area of small velocities which looks like a vortex) and in a large central part of the heated segment above the bottom plate. The transition between the slightly perturbed velocity and temperature fields (when $W_{\phi} = 400 K^{-1}$, for example) and the highly perturbed ones (when $W_{\phi} = 300 K^{-1}$, for example) takes place at $W_{\phi} \approx 325 K^{-1}$ and corresponds to the irregularity observed in section: 3.1.

The stream function presented in Fig. 14 confirms the presence of a vortex (also found in [41] for a turbulent flow of heated air subject to variational optimization) in the initial part of the heated segment as soon as W_{ϕ} is small enough: there is no apparent vortex when $W_{\phi} = 1200 K^{-1}$ and a single vortex is clearly visible if $W_{\phi} = 200 K^{-1}$. for a smaller value like $W_{\phi} = 1 K^{-1}$, the main vortex at the heated zone entry is larger and exhibits a more complex shape. Furthermore, additional recirculating vortexes appear above the heated zone.

A zoom of the velocity vector above and around the central heated zone of the channel is presented in Fig. 15) along with a schematic representation of the main flow directions and of the rotational directions of the vortexes (the + sign meaning that the vortex has a clock-

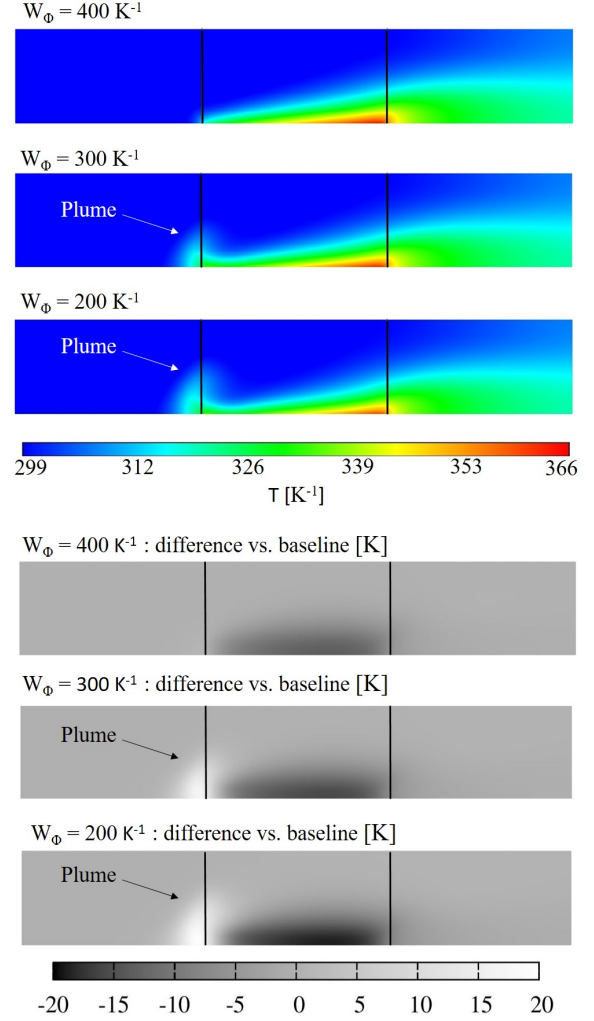


Figure 12: Temperature field for $W_{\phi} = 400 K^{-1}$, $300 K^{-1}$ and $200 K^{-1}$. $Re = 30$. Differences with the baseline are in shades of gray.

wise rotation). The main vortex, located near the entry of the heated zone, collects a part of the heated fluid and transfers it to the accelerated area above the vortex. Then, the flow is stuck towards the heated segment of the bottom plate. As can be seen in Figs. 14 and 15, when $W_{\phi} = 200 K^{-1}$, the center of the main vortex is located just after the beginning abscissa of the heated zone. Nevertheless, for low values of W_{ϕ} , this center is located before this abscissa (this is the case when $W_{\phi} = 1 K^{-1}$, but also when $W_{\phi} = 6 K^{-1}$ for instance). The vertical extension of the main vortex increases when W_{ϕ} decreases and so does the barycentric position of the accelerated area above the vortex: when $W_{\phi} = 1 K^{-1}$ (Fig. 15), this high speed area is very close

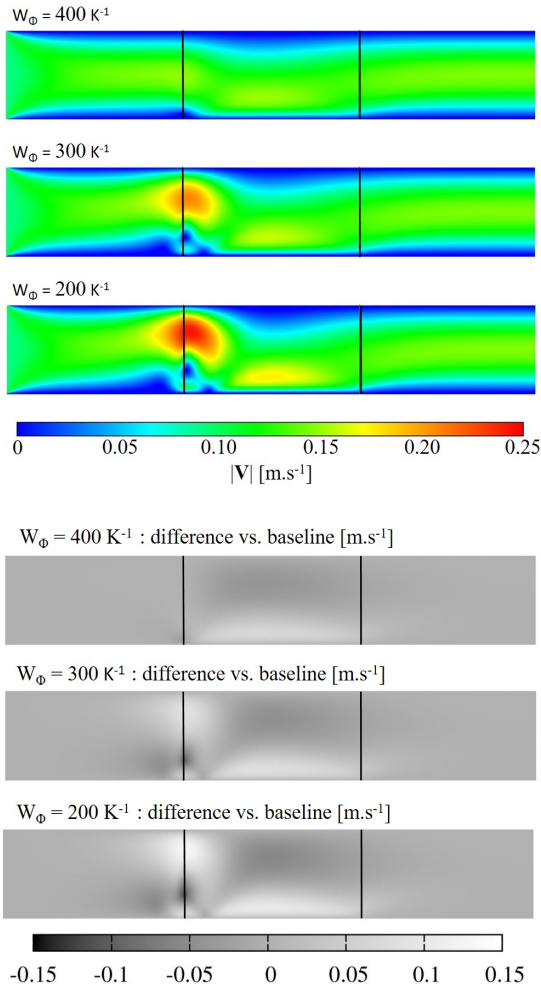


Figure 13: Velocity magnitude field for $W_\phi = 400 K^{-1}$, $300 K^{-1}$ and $200 K^{-1}$. $Re = 30$. Differences with the baseline are in shades of gray.

to the top plate of the channel.

490 The Lagrange multiplier λ_2 field is presented in Fig. 16 when $W_\phi = 200 K^{-1}$. The highest values are concentrated in the first third of the heated area and mainly close to the plate. This is to be related to the magnitude of the corresponding force field F presented in Fig. 17. 495 Indeed, high λ_2 values contribute to the increase of the first term of the expression defining F in Eq. 8 and this term also involves the temperature gradient that reaches high values near the heated plate segment. The main effect of the force field applied in the central third of the channel is to push down the fluid in the direction of the plate and to the starting point of the heated segment. Moreover, the force field tends to squeeze the flow and to crutch the thermal boundary layer above the heated 500 segment of the bottom plate. As can be seen in Figs.

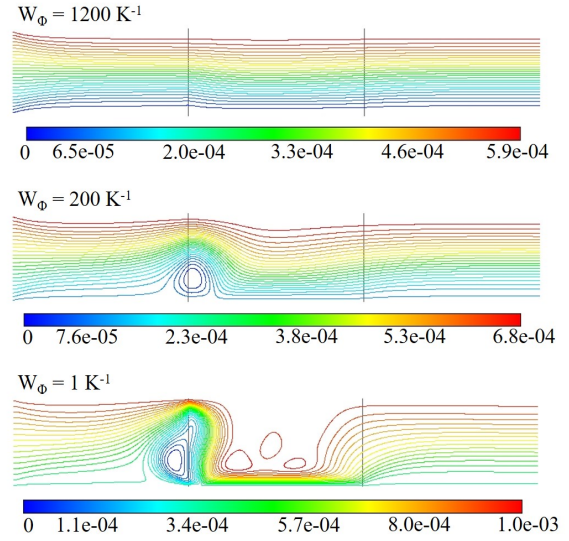


Figure 14: Stream function [$kg.s^{-1}$]. $Re = 30$.

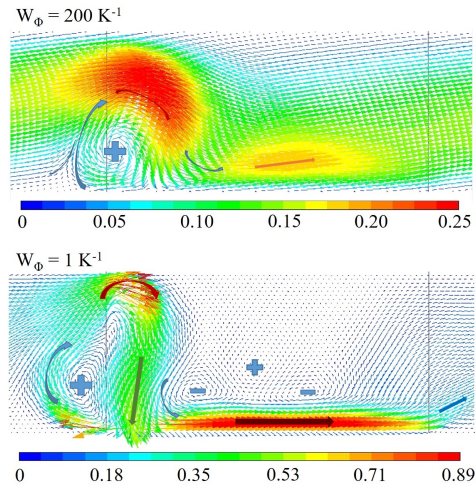


Figure 15: Velocity vector (zoom) with an indication of the main flow directions and of the rotational direction of vortices: "+" means clockwise. $Re = 30$.

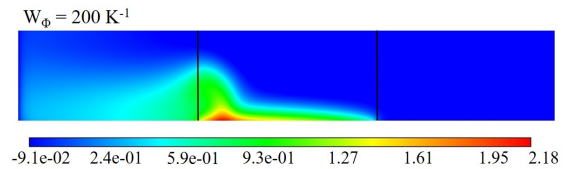


Figure 16: λ_2 Lagrange multiplier [$J.m^{-3}.K^{-2}$] field ($Re = 30$).

13, 14, 15 and 17, there is a strong relationship between the applied force field and the velocity vector.

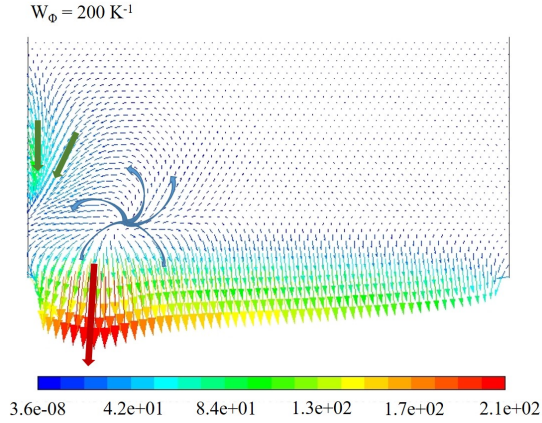


Figure 17: Force field \mathbf{F} applied above the heated segment area [$N.m^{-3}$] ($Re = 30$).

The local entropy generation rate fields by heat conduction and by viscous friction are presented in Figs. 18 and 19 respectively (the latter using a logarithmic color scale for the sake of visibility). Significant entropy generation rates by heat conduction are located above the heated segment and are mainly due to the vertical conduction of heat. A convective trail appears at the exit of the heated zone. As W_ϕ decreases, the region of higher entropy generation rate by heat conduction is flattened and closer to the bottom plate. For values of W_ϕ small enough to make appear the thermal protrusion before the beginning of the heating zone, a plume appears in this area (see figs. 12 and 18 when $W_\phi = 200 K^{-1}$). The behavior of the local entropy generation rate by viscous friction is more complex (Fig. 19). The highest entropy generation rates by viscous friction are located at the channel inlet wall ordinates $y = 0$ and $y = H$ because of the discontinuity of the velocity that changes from U_{in} to zero at the walls. Just after this entry zone, the main viscous dissipation comes generally from areas close to the walls, at least when the velocity field is not too disturbed. Concentrating mainly to the part of the channel located above the heated segment, the perturbation of the entropy generation rate field by viscous friction becomes apparent even for high values of the weighting factor, like $W_\phi = 5900 K^{-1}$ or $W_\phi = 1200 K^{-1}$: the narrow longitudinal region of low entropy generation rate located in the center of the channel is deviated when crossing the entry of the heated zone and even almost broken when $W_\phi = 1200 K^{-1}$. For lower values ($W_\phi = 200 K^{-1}$), the entropy generation rate by viscous friction (and the viscous dissipation) is more perturbed and higher generation rates concentrate above the heated segment but also at the top wall

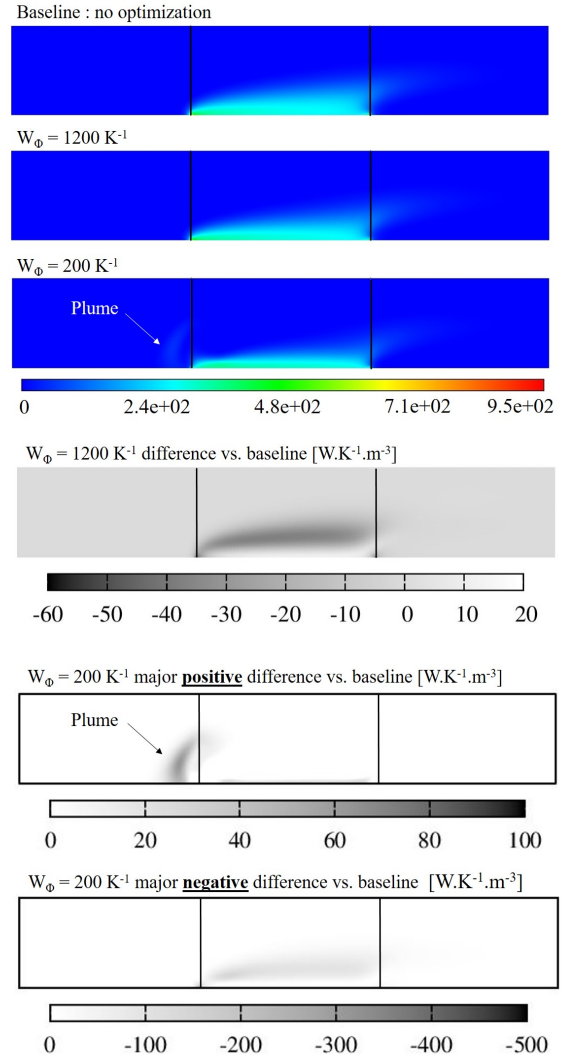


Figure 18: Local entropy generation rate by heat conduction [$W.K^{-1}.m^{-3}$] for $W_\phi = 5900 K^{-1}$, $1200 K^{-1}$, $200 K^{-1}$ and when no optimization is applied. Differences with the baseline are in gray.

around $x = 10 mm$ and along a closed curve enclosing the main velocity vortex. Indeed, the velocity field pattern is the main contributor to the complex shape of the entropy generation rate by viscous friction because the temperature field is simpler and kept in a smaller relative interval of values.

3.3. Key physical quantities

The volume average of the temperature in the channel (Fig. 20) is an increasing function of W_ϕ , while staying in a narrow interval: as an example, when $Re = 30$, the mean temperature is located between $309.8 K$ and $307.9 K$ while W_ϕ decreases from $5900 K^{-1}$ to $6 K^{-1}$.

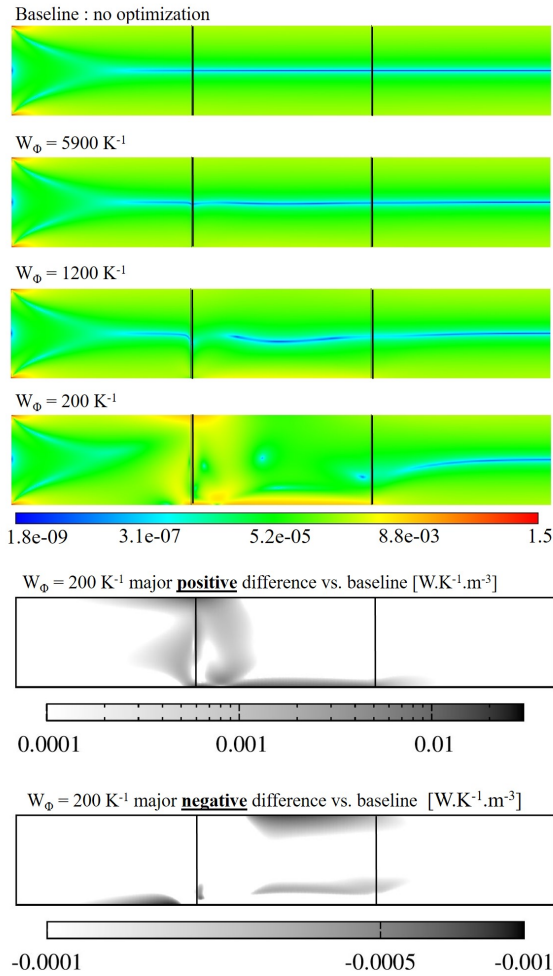


Figure 19: Local entropy generation rate by viscous friction in $[W.K^{-1}.m^{-3}]$ for $W_{\phi} = 5900 K^{-1}$, $1200 K^{-1}$, $200 K^{-1}$ and when no optimization is applied. Color scale is logarithmic. Positive and negative differences with the baseline are in gray.

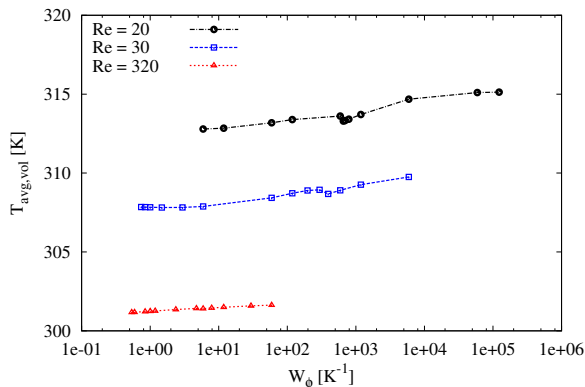


Figure 20: Average temperature in the Channel $[K]$.

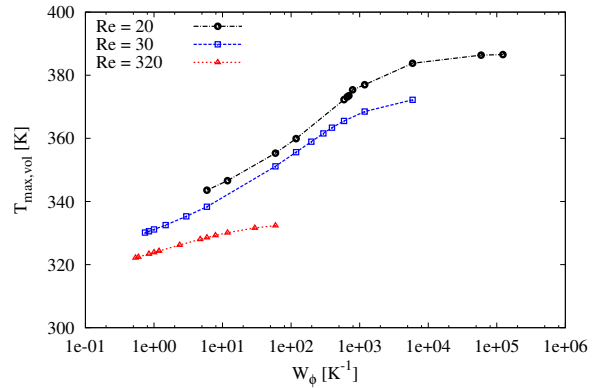


Figure 21: Maximum temperature in the Channel $[K]$.

The maximum temperature inside the channel (Fig. 21) also decreases as W_{ϕ} gets smaller and it is the same for the standard deviation of the temperature that drops from $15.54 K$ to $8.06 K$ over the same range of W_{ϕ} , in accordance with a better thermal mixing due to the applied force field. Higher Reynolds numbers lead to lower maximal and average temperatures: the total injected thermal power is a constant and an increase of the inlet velocity leads to a higher exchange coefficient that induces lower temperature gaps.

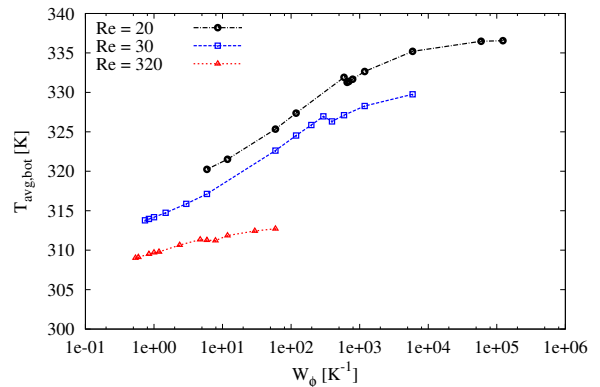


Figure 22: Average temperature on the bottom plate $[K]$.

The average temperature of the heated wall is also lower as W_{ϕ} decreases (Fig. 22) and the same behavior can be observed for the maximum temperature at the same wall (Fig. 23): Using the example of simulations where $Re = 30$, the maximum temperature of the lower wall is $373.5 K$ when no optimization is applied. For a high value of W_{ϕ} like $5900 K^{-1}$, this temperature is $372.2 K$, a value very close to the non-optimized situation. On the other hand, for a smaller weighting factor,

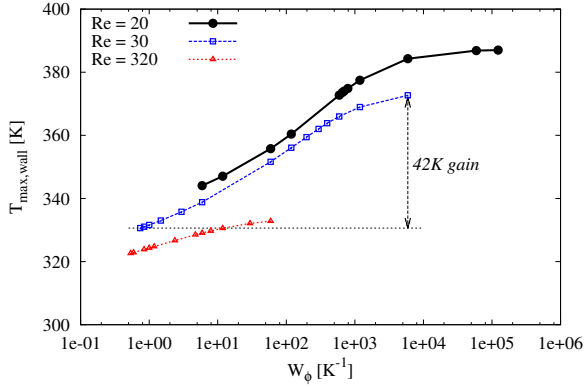


Figure 23: Maximum temperature on the bottom plate [K].

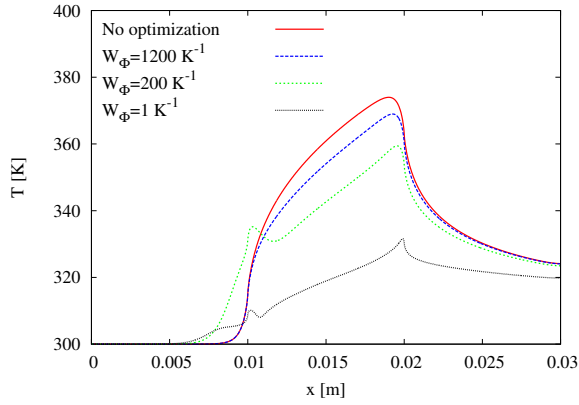


Figure 24: Temperature along the bottom plate [K].

such as $W_{\phi} = 0.74 \text{ K}^{-1}$, the heated plate peak temperature is only 330.1 K , corresponding to a gain of 42K . The temperature profiles of the bottom plate as a function of the abscissa are shown in Fig. 24 for several values of W_{ϕ} and demonstrate the narrowing of the temperature range at the heated plate as W_{ϕ} decreases. The reduction of the maximum temperature and the better thermal homogeneity of the heated plate are an advantage in applications like concentrated solar power where materials are subjected to high temperature stress that can be the cause of damage or accelerate aging due to thermo-mechanical [60] [61] or chemical [62] [63] constraints (oxidation for example [64]).

The average temperature at the outlet of the channel is practically independent on the value of W_{ϕ} (Fig. 25) and is very close to the mass flow averaged temperature at the outlet. The steady flow is incompressible and the fluid properties are constant. As the inlet temperature and the heat flow input into the channel are fixed and as the viscous heating is neglected, the mass flow av-

eraged temperature at the outlet is practically fixed for a given value of the Reynolds number and equals approximately 327 K , 317 K and 301.7 K for $Re = 20$, $Re = 30$ and $Re = 320$ respectively. On the other hand, the smaller the value of W_{ϕ} , the more homogeneous the temperature at the outlet of the channel as demonstrated in Fig. 26.

The different temperature profiles and fields presented above show that the velocity field pattern obtained by variational optimization leads to a better homogeneity of the thermal field, compatible with a reduction in the entropy generation rate in the channel. This improvement is achieved at the cost of an increase in entropy generation by viscous dissipation, which is linked to velocity gradients: the maximum velocity magnitude observed in the channel increases when W_{ϕ} gets smaller (Fig. 27). Its profile is similar in appearance to that of the total viscous dissipation (Fig. 7) or the rate of entropy generation by viscous dissipation (Fig. 6): for large values of W_{ϕ} , the maximum velocity magnitude is practically stable (and close to that which would be observed without optimization). From the transition to disturbed flow regimes, the maximum velocity magnitude in the channel increases rapidly as W_{ϕ} decreases, the slope being higher as the Reynolds number gets higher.

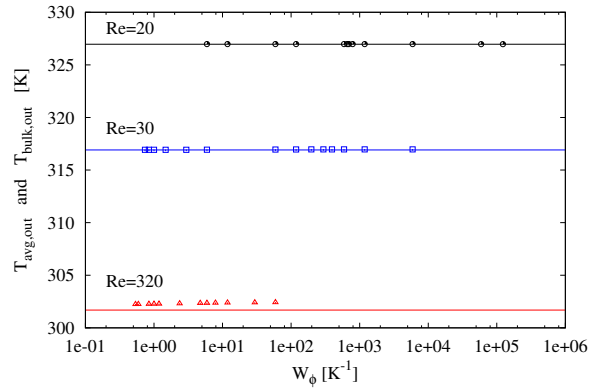


Figure 25: Average temperature at outlet [K]. Horizontal solid lines indicate the mass flow averaged temperature $T_{bulk,out}$.

The heat transfer improvement can be measured through the Nusselt number. The decrease in the entropy generation rate is consistent with the increase in the heat transfer coefficient and the Nusselt number (Fig. 28). When $Re = 30$, the mean Nusselt number computed over the heated segment of the bottom plate (Eqs. 14 and 15, where D_H is the hydraulic diameter and L_q the length of the heated area) is increased from 8.6 to 37.9 as the entropy generation rate in the channel drops from $4.22 \times 10^{-3} \text{ W.K}^{-1}$ to $1.04 \times 10^{-3} \text{ W.K}^{-1}$. For large

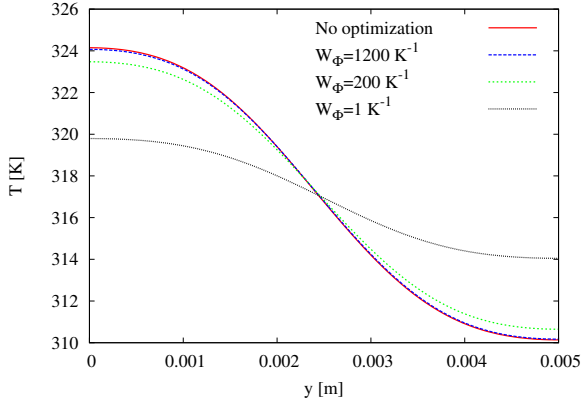


Figure 26: Temperature profile at outlet [K].

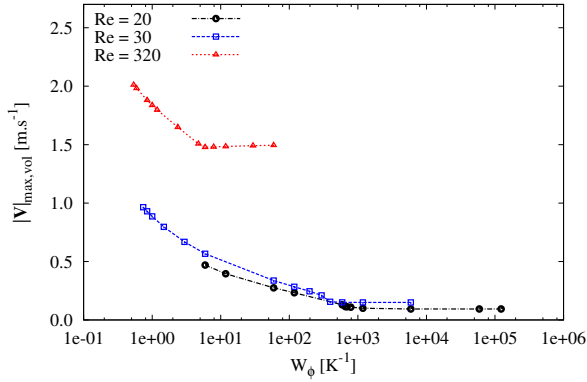


Figure 27: Maximum velocity magnitude in the Channel [m.s⁻¹].

values of W_{ϕ} , while still searching for a reduction in the entropy generation rate, the focus is heavily put on not increasing the viscous dissipation. This results in velocity and thermal fields that are little changed with respect to the case without optimization and the improvement factor is low. As W_{ϕ} decreases, the constraint on the containment of the viscous dissipation is released progressively and the temperature field gets more homogeneous, which leads to a decrease of the entropy generation rate, an increase of the improvement factor I_s (Eq. 13) and consequently an improvement of the Nusselt number.

$$Nu = \frac{hD_H}{k} \quad (14)$$

$$h = \frac{1}{L_q} \int_{\text{heated area}} \frac{q''}{T_{\text{bottom}}(x) - T_{\text{bulk}}(x)} dx \quad (15)$$

Simultaneously, as the entropy generation rate de-

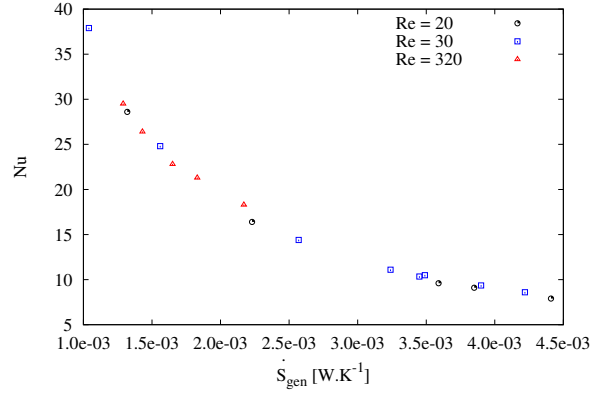


Figure 28: Mean Nusselt number as a function of the total entropy generation rate.

640 creases and the Nusselt number becomes larger, the Fanning friction factor C_f (Eq. 16, where τ_w is the mean shear stress at the bottom plate and V_b the bulk velocity) increases (Fig. 29). In the optimized solutions, the reduced temperature gaps for the same heat flux density lead to increased Nusselt numbers. These optimized solutions also correspond to and homogenization of the temperature field induced by a more complex and accelerated velocity field resulting in more viscous friction at the plate.

$$C_f = \frac{\tau_w}{\frac{1}{2}\rho V_b^2} \quad (16)$$

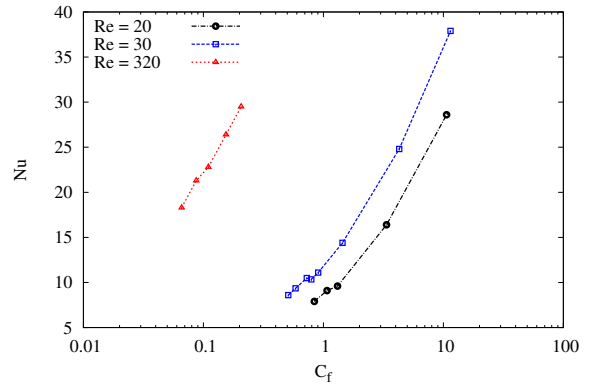


Figure 29: Mean Nusselt number as a function of the mean friction factor C_f .

In the present study, the fluid properties are considered to be constant. However, real gas properties do vary with temperature and this is the case for air within the temperature range observed in the simulations (from

300 K to about 380 K). Compressibility or temperature dependent viscosity and thermal conductivity can influence the particular value of the critical weighting factor that triggers the transition between the different levels of perturbation of the flows. Analyzing the impact of variable fluid properties requires solving more intricate governing equations as the temperature field would additionally impact the flow dynamics. The variational problem would also result in a more complex expression of the body-force field (Eq. 8 and 9 would be modified and more challenging). The study of flows involving a fluid with thermo-dependent properties is a research work in itself and is a natural extension of the present work to be performed in the future.

4. Conclusion

In this paper, convective heat transfer optimization in channel flow is addressed using variational methods applied to an objective functional built as a linear combination of the entropy generation rate in the channel (more precisely, the entropy generation rate by heat conduction, which is overwhelmingly dominant in the cases studied) and the total viscous dissipation, a coefficient that acts as a weighting factor being assigned to the latter. Optimal velocity field patterns are induced by a virtual volume force field that is a solution of the variational problem. Several simulations have been performed, at different Reynolds numbers and for a wide range of weighting factor values, in order to assess the improvement in terms of entropy generation reduction. The resulting velocity, temperature and local entropy generation rate fields are described, as well as the influence of the viscous dissipation function weighting factor on the flow and on the key physical quantities like the average and maximum temperatures in the channel, at the heated plate and at the outlet.

Depending on the value of the weighting factor, the optimized velocity and temperature fields are more or less perturbed by comparison to the case where no optimization is applied and a critical value of this factor determines the transition from low to high-disruption solutions. The higher the Reynolds number, the lower the critical value of the weighting factor. Small values of the weighting factor lead to highly perturbed velocity patterns exhibiting one or more vortexes and a tightening of the flow closer to the heated area. The corresponding thermal field is influenced by this mixing and the temperatures are lower and more homogeneous in the channel, at the heated plate and at the outlet. This improvement is reflected in the total entropy generation

rate that is significantly reduced (the lower the weighting factor, the lower the entropy generation rate in the channel) and in the corresponding increase of the Nusselt number. The reduction in entropy generation rate is done at the expense of an increase of the total viscous dissipation, the velocity magnitudes being higher in the channel and the velocity field being more complex. The entropy generation rate by viscous friction increases alongside but has no effect on the improvement in total entropy generation rate, due to its small order of magnitude. From the application point of view, it is found that a significant wall temperature reduction can be obtained, while maintaining the same power transferred to the fluid. This result shows an increase of heat transfer efficiency at the wall. The weighting factor allows to find a wide range of trade-offs depending on the relative focus put on reducing the entropy generation rate or the total viscous dissipation: from a practical point of view, a designer could select from this range of solutions a sub-set that meets additional technical criteria (e.g. a total mechanical power input limited to a certain value or a maximum hot wall temperature not to be exceeded). Then a selected solution in this sub-set could be picked-up by taking into consideration the practical realization of the velocity pattern (e.g., those with slightly perturbed patterns are likely to be easier to implement than more complex solutions with one or several vortexes).

5. Acknowledgment

This work was supported by French "Investments for the future" ("Investissements d'Avenir") programme managed by the National Agency for Research (ANR) under contract ANR-10-LABX-22-01 (labex SOLSTICE). This project has received funding from the European Union's Horizon 2020 research and innovation programme under grant agreement No 654663, SOLPART project

6. Appendix

In this appendix, the range of values chosen for the weighting parameter W_{Φ} is discussed and the check of key physical quantity balances is presented. A concluding remark identifies results in accordance with other published research works.

The range of values selected for the weighting factor allows to investigate a wide range of trade-offs depending on the relative focus put on reducing the entropy generation rate (small W_{Φ}) or containing the total viscous dissipation (large W_{Φ}), while including the

critical value $W_{\phi,critical}$ that triggers the transition between highly and slightly perturbed flow patterns. For high values of the weighting factor, the first term in the expression of the body-force (Eq. 8) approaches zero and the volume force becomes practically independent on W_{ϕ} . The physical quantities like the total entropy generation rate or the total viscous dissipation present an asymptotic behavior. The highest values of W_{ϕ} presented allow to show this asymptotic behavior (for $Re = 20$ in particular) without continuing towards larger values of little practical interest, especially since the improvement factors are low and decreasing as W_{ϕ} increases (Fig. 3). For small values of W_{ϕ} , the first term in the expression of the body-force becomes significant and creates a coupling between the velocity and the temperature fields. As W_{ϕ} decreases, the velocity field becomes more and more complex and the maximum velocity in the flow increases, which ends by requiring finer meshes and larger computation times to ensure the numerical convergence of the simulations. In this study we went down to $W_{\phi} \approx 0.5 K^{-1}$ (for $Re = 320$) and the total range of values of the weighting factor spans across six orders of magnitude, while staying into accessible computation times.

The balance of mass, kinetic energy, enthalpy and entropy have been checked: for $Re = 20$ and $W_{\phi} = 200 K^{-1}$ the net mass flux is zero to the nearest $10^{-7} kg.s^{-1}$. The kinetic energy is balanced with an error of 0.16% of the total viscous dissipation. The bulk temperature at the outlet deduced from the enthalpy balance and computed directly at the outlet are identical to the nearest mK . The entropy is balanced with an error of 0.08% of the total entropy generation rate. These balances show that the numerical errors are small compared to the quantities presented (total viscous dissipation, total entropy generation rate, temperatures).

The results of the present study are qualitatively in accordance with [45] and [41], which deal with convective transfer enhancement: the optimized velocity fields can exhibit a vortex and result in a better homogenization of the scalar field while the dropping entropy generation rate (which is lower in the optimized cases) changes in the opposite direction to the rising total viscous dissipation.

7. References

- [1] S.-K. Moon, J. Kim, S. Cho, B. J. Kim, J. K. Park, Y.-J. Youn, C.-H. Song, Single-phase convective heat transfer enhancement by spacer grids in a rod bundle, *Journal of Nuclear Science and Technology* 51:4 (2014) 543–557. doi:10.1080/00223131.2014.881726.
- [2] C. Chang, C. Xu, Z. Y. Wu, X. Li, Q. Q. Zhang, Z. F. Wang, Heat transfer enhancement and performance of solar thermal absorber tubes with circumferentially non-uniform heat flux, *Energy Procedia - International Conference on Concentrating Solar Power and Chemical Energy Systems, SolarPACES 2014* 69 (2015) 320–327. doi:10.1016/j.egypro.2015.03.036.
- [3] X. Daguene-Frick, J. M. Foucaut, S. Couderc, A. Toutant, G. Olalde, Experimental analysis of the turbulent flow behavior of a textured surface proposed for asymmetric heat exchangers, *Flow Turbulence and Combustion* 89 (2012) 149–169. doi:10.1007/s10494-012-9387-y.
- [4] A. Colleoni, A. Toutant, G. Olalde, J.-M. Foucaut, Optimization of winglet vortex generators combined with riblets for wall/fluid heat exchange enhancement, *Applied Thermal Engineering* 50 (2013) 1092–1100. doi:10.1016/j.applthermaleng.2012.08.036.
- [5] J. M. Avellaneda, F. Bataille, A. Toutant, DNS of turbulent low Mach channel flow under asymmetric high temperature gradient: Effect of thermal boundary condition on turbulence statistics, *International Journal of Heat and Fluid Flow* 77 (2019) 40–47. doi:10.1016/j.ijheatfluidflow.2019.03.002.
- [6] D. Dupuy, A. Toutant, F. Bataille, Turbulence kinetic energy exchanges in flows with highly variable fluid properties, *Journal of Fluid Mechanics* 834 (2018) 5–54. doi:10.1017/jfm.2017.729.
- [7] D. Dupuy, A. Toutant, F. Bataille, Effect of the reynolds number on turbulence kinetic energy exchanges in flows with highly variable fluid properties, *Physics of Fluids* 31(1) (2019) 015104. doi:10.1063/1.5080769.
- [8] L. Liebenberg, J. P. Meyer, In-tube passive heat transfer enhancement in the process industry, *Applied Thermal Engineering* 27 (2007) 2713–2726. doi:10.1016/j.applthermaleng.2007.06.003.
- [9] A. E. Bergles, The implications and challenges of enhanced heat transfer for the chemical process industries, *Chemical Engineering Research and Design* 79(4) (2001) 437–444. doi:10.1205/026387601750282562.
- [10] R. Li, Numerical simulation on forced convection cooling of horizontal ionic wind with multi-electrodes, *16th International Refrigeration and Air Conditioning Conference*, July 11-14, 2016 - Paper 1696. URL <http://docs.lib.purdue.edu/iracc/1696>
- [11] A. M. Hussein, R. A. Bakar, K. Kadirgama, Study of forced convection nanofluid heat transfer in the automotive cooling system, *Case Studies in Thermal Engineering* 2 (2014) 50–61. doi:10.1016/j.csite.2013.12.001.
- [12] A. S. Sunden, Z. Wu, D. Huang, Comparison of heat transfer characteristics of aviation kerosene flowing in smooth and enhanced mini tubes at supercritical pressures, *International Journal of Numerical Methods for Heat & Fluid Flow* 24(3/4) (2016) 1289–1308. doi:10.1108/HFF-12-2015-0538.
- [13] L. Lal, M. Miscevic, P. Lavielle, M. Amokrane, F. Pigache, F. Topin, B. Nogarde, L. Tadrist, An overview of heat transfer enhancement methods and new perspectives: Focus on active methods using electroactive materials, *International Journal of Heat and Mass Transfer* 61 (2013) 505–524. doi:10.1016/j.ijheatmasstransfer.2013.01.083.
- [14] O. Bulliard-Sauret, S. Ferrouillat, L. Vignal, A. Momponteil, Heat transfer enhancement using 2 MHz ultrasound, *Ultrasonics - Sonochemistry* 39 (2017) 232–271. doi:10.1016/j.ultsonch.2017.04.021.
- [15] S.-J. Yang, A numerical investigation of heat transfer enhancement for electronic devices using an oscillating vortex generator, *Numerical Heat Transfer - Part A: Applications* 42:3 (2017) 269–284. doi:10.1080/10407780290059549.

- [16] P. Kumar, K. Schmidmayer, F. Topin, M. Miscevic, Heat transfer enhancement by dynamic corrugated heat exchanger wall: Numerical study, *Journal of Physics: Conference Series*, 7th European Thermal-Sciences Conference (Eurotherm2016) 032061. doi:10.1088/1742-6596/745/3/032061.
- [17] S. Dey, D. Chakraborty, Enhancement of convective cooling using oscillating fins, *International Communications in Heat and Mass Transfer* 36 (2009) 508–212. doi:10.1016/j.icheatmasstransfer.2009.01.018.
- [18] I. Nastase, F. Bode, Impinging jets a short review on strategies for heat transfer enhancement, *E3S Web of Conferences* 32, 01013. doi:10.1051/e3sconf/20183201013.
- [19] K. Oyakawa, A. Umdea, M. D. Islam, N. Saji, S. Matsuda, Flow structure and heat transfer of impingement jet, *Heat Mass Transfer* 46(1) (2009) 53–61. doi:10.1007/s00231-009-0543-4.
- [20] B. Horacek, K. T. Kiger, J. Kim, Single nozzle spray cooling heat transfer mechanisms, *International Journal of Heat and Mass Transfer* 48 (2005) 1425–1438. doi:10.1016/j.ijheatmasstransfer.2004.10.026.
- [21] J. Kim, Spray cooling heat transfer: The state of the art, *International Journal of Heat and Fluid Flow* 28 (2007) 753–767. doi:10.1016/j.ijheatfluidflow.2006.09.003.
- [22] S. Laohalerdecha, P. Naphon, S. Wongwises, A review of electrohydrodynamic enhancement of heat transfer, *Renewable and Sustainable Energy Reviews* 11 (2007) 858–876. doi:10.1016/j.rser.2005.07.002.
- [23] B. Kumar, G. P. Srivastava, M. Kumar, A. K. Patil, A review of heat transfer and fluid flow mechanism in heat exchanger tube with inserts, *Chemical Engineering and Processing - Process Intensification* 123 (2018) 126–137. doi:10.1016/j.ccep.2017.11.007.
- [24] S. Liu, M. Sakr, A comprehensive review on passive heat transfer enhancements in pipe exchangers, *Renewable and Sustainable Energy Reviews* 19 (2013) 64–81. doi:10.1016/j.rser.2012.11.021.
- [25] P. Chakraborty, T. Ma, L. Cao, Y. Wang, Significantly enhanced convective heat transfer through surface modification in nanochannels, *International Journal of Heat and Mass Transfer* 136 (2019) 702–708. doi:10.1016/j.ijheatmasstransfer.2019.03.053.
- [26] M. Everts, S. R. Ayres, F. A. M. Houwer, C. P. Vanderwagen, N. M. Kotze, J. P. Meyer, The influence of surface roughness on heat transfer in the transitional flow regime, *Proceedings of the 15th International Heat Transfer Conference IHTC-15*, August 10-15, 2014, Kyoto, Japan (2014) 1626–1637. doi:10.1615/IHTC15.cnv.008338.
- [27] H. Olia, M. Torabi, M. Bahiraei, M. H. Ahmadi, M. Goodarzi, M. R. Safaei, Application of nanofluids in thermal performance enhancement of parabolic trough solar collector: State of the art, *Applied Sciences* 9(3)463. doi:10.3390/app9030463.
- [28] M. Gupta, N. Arora, R. Kumar, S. Kumar, N. Dilbaghi, A comprehensive review of experimental investigations of forced convective heat transfer characteristics for various nanofluids, *International Journal of Mechanical and Materials Engineering* 9:11. doi:10.1186/s40712-014-0011-x.
- [29] S. Kaka, A. Pramanjaroenkij, A comprehensive review of experimental investigations of forced convective heat transfer characteristics for various nanofluids, *Review of convective heat transfer enhancement with nanofluids* 52 (2009) 3187–3196. doi:10.1016/j.ijheatmasstransfer.2009.02.006.
- [30] E. F. Akyrek, K. Gelis, B. Sahin, M. Eyyhan, Experimental analysis for heat transfer of nanoflow with wire coil turbulators in a concentric tube heat exchanger, *Results in Physics* 9 (2018) 376–389. doi:10.1016/j.rinp.2018.02.067.
- [31] K. Liu, C. P. Titan, L. A. Carrilho, J. A. Khan, Enhancement of heat transfer performance in nuclear fuel rod using nanofluids and surface roughness technique, *ASME International Mechanical Engineering Congress and Exposition*, Volume 8B: Heat Transfer and Thermal Engineering, V08BT10A011. doi:10.1115/IMECE2015-51476.
- [32] A. Benabderrahmane, A. Miloud, L. Samir, B. Abdelylah, J. P. Solano, Heat transfer enhancement in a parabolic trough solar receiver using longitudinal fins and nanofluids, *Journal of Thermal Science* 25(5) (2016) 410–417. doi:10.1007/s11630-016-0878-3.
- [33] S. Li, W. Kong, H. Zhang, F. Sabatier, R. Ansart, G. Flamant, J. Baeyens, The fluidized bed air heat exchanger in a hybrid Brayton-cycle solar power plant, *AIP Conference Proceedings* 2126, 140002 (2019). doi:10.1063/1.5117650.
- [34] A. Gallo, J. Spelling, M. Romero, J. Gonzalez-Aguilar, Preliminary design and performance analysis of a multi-megawatt scale dense particle suspension receiver, *Energy Procedia - International Conference on Concentrating Solar Power and Chemical Energy Systems SolarPACES 2014* 69 (2015) 388–397. doi:10.1016/j.egypro.2015.03.045.
- [35] G. Flamant, D. Gauthier, H. Benoit, J. L. Sans, R. Garcia, B. Boissire, R. Ansart, M. Hemati, Dense suspension of solid particles as a new heat transfer fluid for concentrated solar thermal plants: On-sun proof of concept, *Chemical Engineering Science* 102 (2013) 567–576. doi:10.1016/j.ces.2013.08.051.
- [36] M. S. Baba, A. V. Sita Rama Raju, M. Baghvant Rao, Heat transfer enhancement and pressure drop of Fe_3O_4 -water nanofluid in a double tube counter flow heat exchanger with internal longitudinal fins, *Case Studies in Thermal Engineering* 12 (2018) 600–607. doi:10.1016/j.csite.2018.08.001.
- [37] S. W. Chang, T.-M. Liu, K. F. Chiang, G. F. Hong, Heat transfer and pressure drop in rectangular channel with compound roughness of v-shaped ribs and deepened scales, *International Journal of Heat and Mass Transfer* 51(3-4) (2008) 457–468. doi:10.1016/j.ijheatmasstransfer.2007.05.010.
- [38] A. Bejan, *Entropy generation minimization*, CRC Press, 1996, ISBN: 0-8493-9651-4.
- [39] A. Bejan, Entropy generation minimization: the new thermodynamics of finite-sized devices and finite-time processes, *Journal of Applied Physics* 79(3) (1996) 1191–1218. doi:10.1063/1.362674.
- [40] T. A. Jankowski, Minimizing entropy generation in internal flows by adjusting the shape of the cross-section, *International Journal of Heat and Mass Transfer* 52 (2009) 3439–3445. doi:10.1016/j.ijheatmasstransfer.2009.03.016.
- [41] Q. Li, X. Yuan, P. Neveu, G. Flamant, L. Luo, A novel optimization approach to convective heat transfer enhancement for solar receivers, *Chemical Engineering Science* 116 (2014) 806–816. doi:10.1016/j.ces.2014.05.051.
- [42] J. M. Avellaneda, S. Jia, P. Neveu, F. Bataille, X. Yuan, G. Flamant, Similarities between heat and mass transfer enhancement in convective flow, using variational optimization technique, *International Heat Transfer Conference 16*, 2018. 10-15 August, Beijing, China (2018) 2715–2722. doi:10.1615/IHTC16.cov.021341.
- [43] M. M. Awad, The science and the history of the two bejan numbers, *International Journal of Heat and Mass Transfer* 94 (2016) 101–103. doi:10.1016/j.ijheatmasstransfer.2015.11.073.
- [44] R. L. Panton, *Incompressible Flow*, Wiley, 2013, ISBN: 9781118013434. doi:10.1002/9781118713075.
- [45] S. Jia, C. Zhang, X. Yuan, K.-T. Yu, An optimization approach to find the thermodynamic limit on convective mass transfer enhancement for a given viscous dissipation, *Chemical Engineer-*

- ing Science 146 (2016) 26–34. doi:10.1016/j.ces.2016.01.059.
- [46] L. R. Glicksman, J. H. Lienhard V, Modeling and approximation in heat transfer, Cambridge University Press, 2016, ISBN: 978-1-107-01217-2.
- 1000 [47] M. J. K. Madapati, Effect of axial conduction and viscous dissipation on heat transfer for laminar flow through a circular pipe, Perspectives in Science 8 (2016) 61–65. doi:10.1016/j.pisc.2016.03.008.
- 1005 [48] R. B. Bird, W. E. Stewart, E. N. Lightfoot, Transport phenomena, 2nd Edition, John Wiley & Sons, 2002, ISBN: ISBN: 0-471-41077-2.
- [49] D. Li, Encyclopedia of microfluidics and nanofluidic, 2nd Edition, Springer, 2015, ISBN: 978-1-4614-5488-5.
- 1010 [50] T. N. Aynur, L. Kuddusi, N. Egrican, Viscous dissipation effect on heat transfer characteristics of rectangular microchannels under slip flow regime and H1 boundary conditions, Heat Mass Transfer 42 (2006) 1093–1101. doi:10.1007/s00231-005-0075-5.
- 1015 [51] M. R. Romano, F. Cuomo, N. Massarotti, A. Mauro, M. Salahudeen, C. Costagliola, L. Ambrosone, Temperature effect on rheological behavior of silicone oils. a model for the viscous heating, The Journal of Physical Chemistry B 121 (2017) 7048–7054. doi:10.1021/acs.jpcc.7b03351.
- 1020 [52] S. S. Rao, Engineering Optimization, John Wiley & Sons, Hoboken, New Jersey, 2009, ISBN: 978-0-470-18352-6.
- [53] I. M. Gelfand, S. V. Fomin, Calculus of variations, Prentice-Hall, Englewood Cliffs, New Jersey, 1963, ISBN: 978-0-486-41448-5.
- 1025 [54] J. L. Troutman, Variational calculus and optimal control, Springer, 1996, ISBN: 978-1-4612-6887-1. doi:10.1007/978-1-4612-0737-5.
- [55] S. V. Patankar, A. Spadling, A calculation procedure for heat, mass and momentum transfer in three-dimensional parabolic flows, International Journal of Heat and Mass Transfer 15(10) (1972) 1787–1806. doi:10.1016/0017-9310(72)90054-3.
- 1030 [56] A. Inc., FLUENT 15.0 user's guide, SAS IP, 2013.
- [57] X. Cao, S. Jia, Y. Luo, X. Yuan, Z. Qi, K.-T. Yu, Multi-objective optimization method for enhancing chemical reaction process, Chemical Engineering Science 195 (2019) 494–506. doi:10.1016/j.ces.2018.09.048.
- 1035 [58] X. Cao, S. Jia, J.-M. Avellaneda, Y. Luo, X. Yuan, G. Flamant, K.-T. Yu, An optimization method to find the thermodynamic limit on enhancement of solar thermal decomposition of methane, International Journal of Hydrogen Energy 44(31) (2019) 16164–16175. doi:10.1016/j.ijhydene.2019.04.261.
- 1040 [59] H. Schlichting, Boundary layer theory, 9th Edition, Springer, 2017, ISBN: 978-3-662-52917-1. doi:10.1007/978-3-662-52919-5.
- 1045 [60] Y. Lalau, O. Faugeroux, B. Claudet, E. Guillot, D. Andre, M. Huger, A. Proust, T. Chotard, A method for experimental thermo-mechanical aging of materials submitted to concentrated solar irradiation, Solar Energy Materials and Solar Cells 192 (2019) 161–169. doi:10.1016/j.solmat.2018.12.017.
- 1050 [61] A. Montoya, M. R. Rodriguez-Sanchez, J. Lopez-Puente, D. Santana, Thermal and mechanical stresses in a solar central receiver, Renewable Energy and Power Quality Journal International Conference on Renewable Energies and Power Quality (ICREPQ18), 2018. doi:10.24084/repqj16.376.
- 1055 [62] O. Raccurt, F. Matino, A. Disdier, J. Braillon, A. Stollo, D. Bourdon, A. Maccari, In air durability study of solar selective coating for parabolic trough technology, AIP Conference Proceedings 1850, 130010 (2017). doi:10.1063/1.4984504.
- 1060 [63] B. Pierrat, M. Balat-Pichelin, L. Silvestroni, D. Sciti, High temperature oxidation of ZrC20%MoSi2 in air for future solar receivers, Solar Energy Materials & Solar Cells 95 (2011) 2228–2237. doi:10.1016/j.solmat.2011.03.028.
- [64] T. Galiullin, B. Gobereit, D. Naumenko, R. Buck, L. Amsbeck, M. Neises-von Puttkamer, W. J. Quadakkers, High temperature oxidation and erosion of candidate materials for particle receivers of concentrated solar power tower systems, Solar Energy 188 (2019) 883–889. doi:10.1016/j.solener.2019.06.057.

1070 **Nomenclature**

	\mathbf{F}	Volume force vector by unit of volume [$N.m^{-3}$]
	\mathbf{V}	Velocity vector [$m.s^{-1}$]
	\dot{S}_{gen}'''	Local entropy generation rate [$W.K^{-1}.m^{-3}$] (eq. 4)
1075	$\dot{S}_{gen,c}$	Heat conduction entropy generation rate in the channel [$W.K^{-1}$]
	$\dot{S}_{gen,f}$	Viscous friction entropy generation rate in the channel [$W.K^{-1}$]
1080	\dot{S}_{gen}	Total entropy generation rate in the channel [$W.K^{-1}$]
	λ_i	Lagrange multiplier
	μ	Dynamic viscosity [$Pa.s$]
	Φ	Viscous dissipation function [$W.m^{-3}$] (eq. 5)
	Φ_{tot}	Total viscous dissipation in the channel [W]
1085	ρ	Density [$kg.m^{-3}$]
	C_p	Thermal capacity [$J.kg^{-1}.K^{-1}$]
	I_s	Improvement factor (Eq. 13)
	J, J^*	Objective functional and Lagrangian criterion respectively [$W.K^{-1}$]
1090	k	Thermal conductivity [$W.m^{-1}.K^{-1}$]
	P	Pressure [Pa]
	q''	Heat flux density [$W.m^{-2}$]
	Re	Reynolds number (based upon the channel height)
1095	T_{in}	Inlet temperature [K]
	u, v	Longitudinal and normal components of the ve- locity [$m.s^{-1}$]
	V_{in}	Inlet (longitudinal) velocity [$m.s^{-1}$]
1100	W_{Φ}	Weighting factor in objective functional and Lagrangian criterion [K^{-1}]
	x, y	Longitudinal and normal coordinates [m]
	T	Temperature [K]